

Simulating Three-Dimensional Hydrodynamics on a Cellular Automata Machine

Christopher Adler,^{1,2} Bruce Boghosian,³ Eirik G. Flekkøy,^{1,4}
Norman Margolus,⁵ and Daniel H. Rothman¹

Received November 30, 1994; final April 10, 1995

We demonstrate how three-dimensional fluid flow simulations can be carried out on the Cellular Automata Machine 8 (CAM-8), a special-purpose computer for cellular automata computations. The principal algorithmic innovation is the use of a lattice gas model with a 16-bit collision operator that is specially adapted to the machine architecture. It is shown how the collision rules can be optimized to obtain a low viscosity of the fluid. Predictions of the viscosity based on a Boltzmann approximation agree well with measurements of the viscosity made on CAM-8. Several test simulations of flows in simple geometries—channels, pipes, and a cubic array of spheres—are carried out. Measurements of average flux in these geometries compare well with theoretical predictions.

KEY WORDS: Lattice gases; cellular automata; special-purpose computers; flow through porous media.

1. INTRODUCTION

A cellular automaton is a system of discrete variables on a lattice which is updated according to some simple and local rule.^(1,2) Though applications of such models range from physics to biology to social science,⁽³⁾ one of the most exciting areas of interest in recent years has been hydrodynamics.

¹ Department of Earth, Atmospheric, and Planetary Sciences, Massachusetts Institute of Technology, Cambridge, Massachusetts 02139.

² Current address: Box 90665, Department of Music, Duke University, Durham, North Carolina 27708-0665.

³ Center for Computational Science, Boston University, Boston, Massachusetts 02215.

⁴ Current address: Laboratoire de Physique Mécanique des Milieux Hétérogènes, Ecole Supérieure de Physique et Chimie Industrielle, 75005 Paris France.

⁵ Laboratory for Computer Science, Massachusetts Institute of Technology, Cambridge, Massachusetts 02139.

This interest derives from the discovery by Frisch, Hasslacher, and Pomeau in 1986 that discrete cellular automaton models of fluids, known specifically as *lattice-gas automata*, may be constructed for the numerical solution of the Navier–Stokes equations.^(4, 5) Since their introduction, lattice gases have been used to study a variety of problems in hydrodynamics. Perhaps the greatest interest in the method is for the simulation of problems that either involve complex boundaries, such as porous media,⁽⁶⁾ or complex fluids, such as suspensions^(7, 8) or immiscible mixtures.^(9–11)

As in most other endeavors in computational physics, there is a great need for fast, low-cost simulations. Indeed, it has long been recognized that the simplicity of lattice gases allows them to be simulated on special-purpose hardware, called “cellular automata machines.”^(12, 13, 2) Such machines have been constructed for the simulation of general cellular automata, and have been applied to a variety of systems. They combine the performance of supercomputers with the hardware simplicity of a personal computer or workstation for these particular applications.

In this paper we describe an implementation of a three-dimensional lattice-gas model⁽¹⁴⁾ on a new cellular automata machine called CAM-8.^(15, 16) CAM-8 retains the high performance-to-cost ratio of previous cellular automata machines, but with considerably increased flexibility. It is precisely this flexibility which makes it attractive for simulating lattice gases.

Lattice gases (as well as other cellular automata) may be simulated by the application of a lookup table, which gives an output state from the input state at every site of the lattice. The size of this table increases with the number of degrees of freedom per site. For this reason lattice gases for three-dimensional hydrodynamics,⁽¹⁴⁾ which typically require 24 bits of state (and hence 2^{24} possible states) per site, have proved challenging to implement in situations where memory is limited, such as on a distributed-memory multiprocessor. Following the pioneering work of Hénon,^(17–19) a considerable reduction of table size was achieved by Somers and Rem.⁽²⁰⁾ Precisely what algorithm and collision table to use, however, remains a machine-dependent question. Because the CAM-8 allows one to work most efficiently with units of 16 bits of state per site at any instant of time, we have chosen to design a new collision strategy built upon successive 16-bit table lookups. Our results, in terms of minimization of viscosity (and thus maximization of efficiency for the types of simulations that interest us) are roughly comparable to those obtained by previous workers.

The outline of the paper is as follows. We first briefly summarize the principal architectural features of the CAM-8. We then review the key features of the face-centered hypercubic (FCHC) lattice-gas model upon which our implementation is based. Next, we show how the collision step of the FCHC lattice gas can be broken down into operations that involve

no more than 16 bits at a time. We also show how the collision rules can be optimized in a simple way to give a small viscosity. We compare our theoretical predictions of the viscosity to results obtained by numerical simulation on CAM-8. Finally, we report a number of test simulations of flow through channels, pipes, and a periodic array of spheres and compare our results to analytic predictions. Our goal in this latter exercise is to provide some practical guidelines for the application of our methods to the measurement of the permeability of disordered media.

2. CAM-8

CAM-8 is an indefinitely scalable parallel computer optimized for the large-scale simulation of three-dimensional cellular automata (CA) systems. It emphasizes simulation size, flexibility, and cost efficiency, rather than ultimate performance. This emphasis leads to a *virtual processor* design.⁽¹⁶⁾

2.1. Hardware Overview

In CAM-8, each processor simulates the operation of up to millions of spatial sites, with the site data stored in conventional DRAM-memory chips. This DRAM is scanned sequentially in an addressing pattern that maximizes the speed of access, and data are read, updated (by SRAM-memory table lookup), and put back. This update cycle, which is illustrated in Fig. 1, left, resembles the operation of a video framebuffer, and indeed CAM-8 is genetically more closely related to framebuffer hardware than to conventional microprocessors.

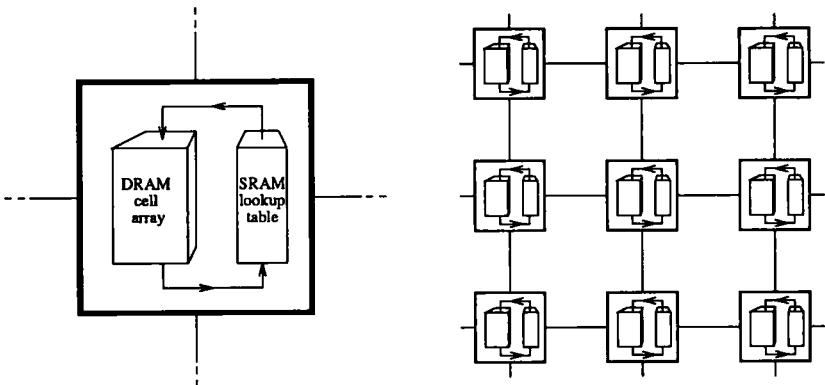


Fig. 1. CAM-8 system diagram. On the left is a single processing node with dynamic random access memory (DRAM) site data flowing through a static random access memory (SRAM) lookup table. On the right is a spatial array of CAM8 nodes.

Figure 1, right, schematically illustrates an array of CAM-8 processing nodes (the array is actually three dimensional in the machine). A uniform spatial calculation is handled in parallel by these nodes, with each node containing an equal “chunk” of the space. In the diagram the solid lines between nodes indicate a local mesh interconnection, used for spatial data movement between processors. Since each processor handles millions of spatial sites, but only one at a time, these mesh wires are time shared among millions of sites. The consequent reduction in interconnect compared to what would be needed in a fully parallel machine makes large three-dimensional simulations practical. There is also a communications network (not shown) connecting all nodes to a front-end workstation that controls the CAM-8 machine. The workstation uses this network to broadcast simulation parameters to all or some of the processing nodes.

Although the initial CAM-8 chip design accommodates machines with many thousands of processing nodes, the first prototypes had only eight nodes. All of the simulations discussed in this paper were performed on such an eight node prototype, which has about the same amount and quality of hardware as one might find in a low-end workstation: 2 Mbytes of SRAM, 64 Mbytes of DRAM, about two million gates of 1.2-micron CMOS logic, with the whole thing running at 25 MHz.

2.2. Programmable Resources

CAM-8 is a virtual-processor simulator of a fully parallel CA space. Its virtual nature makes it possible to reconfigure and redirect its computing resources, allowing the programmer to directly control parameters such as:

- Number of dimensions
- Size and shape of the space
- Number of bits at a site
- Directions and distances of data movement
- Rules of data interaction (lookup tables)

The most novel facet of CAM-8’s operation is the data movement, which is lattice gas like. Corresponding bits, one from each spatial site, constitute a *bit-field*: each bit-field can be shifted in any direction by a chosen amount. The direction is chosen independently for each bit-field, and the amount can be quite large—up to a few thousand positions.⁶ Data movements are uniform across the entire space—the hardware hides the fact that the space is divided up among separate processor nodes.

⁶ Such large spatial shifts are useful in generating the high-quality random variables that are needed by statistical mechanics simulations.

The hardware only allows 16 separate bit-fields to be manipulated at a time. The 16 bits that “collide” at a given spatial site (i.e., those that land there due to their bit-field shifts) are replaced with a new value given by a lookup table. In fact, all data interaction is performed by 16-input/16-output lookup tables. Interactions that involve more than 16 bits at each site must be synthesized as a sequence of 16-bit interactions.

The lookup tables in the hardware are double buffered: this means that while one table is being actively used to scan all the sites and update each in turn, the front-end workstation can broadcast the table that will be used next. Since the data movement is controlled by a few pointers within each processor, these movements can be changed quickly from one scan to the next. Thus there is very little overhead involved in applying a different lookup table *and* a different set of bit-field movements at every scan of the space.

Finally, we note that most of our data analysis and data collection is performed directly by dedicated statistics-gathering hardware. The CA space is split up into bins of a chosen size and lookup tables are used to evaluate a function on each of the sites in each bin. These function data are collected by event counters and are continuously reported back to the front end as the simulation runs.

3. THE FCHC LATTICE GAS

Two fluids with quite different microscopic interactions may still have the same macroscopic behavior. The reason for this is that the form of the macroscopic equations of motion that describe this behavior depend only on the conservation laws obeyed by these interactions and not on their detailed form. This was one of the main motivations for the introduction of lattice-gas automata as a method to simulate fluid flow.

A lattice gas models a fluid as a large number of particles undergoing simple interactions that conserve mass and momentum. While the aim of molecular dynamics is to simulate the real physics at the molecular, or microscopic, scale, the microworld of lattice gases is fictitious. Nevertheless, realistic macroscopic behavior is recovered when space and time averages are performed.

One of the first lattice-gas models was introduced by Hardy *et al.* in 1976.⁽²¹⁾ This model, constructed on a square lattice, succeeded in describing isotropically propagating sound waves, and, if two particle species were introduced, diffusion. The hydrodynamics of this model, however, was anisotropic, as was the damping of the sound waves.

The simplest and first lattice-gas model that produced isotropic two-dimensional hydrodynamic behavior was introduced on a triangular lattice

by Frisch *et al.* in 1986.^(4, 5, 22, 11) The triangular lattice is crucial for the isotropy of the flow dynamics, which, technically, relies on the isotropy of the second- and fourth-order tensors constructed from the basis vectors of the lattice. In three dimensions no regular lattice with this property exists. However, the four-dimensional face-centered hypercubic (FCHC) lattice has the required symmetry,⁽¹⁴⁾ as do its multispeed projections to three dimensions. The latter case is isotropic because some of the lattice vectors have multiplicity two.

3.1. Description of the FCHC Lattice

The FCHC lattice is formed from the four basis vectors $(\pm 1, \pm 1, 0, 0)$ and the 20 additional vectors obtained by permuting the components of these vectors. The FCHC lattice thus has a total of 24 basis vectors, and we list these as follows:

$$\begin{array}{ccc}
 A & B & C \\
 \begin{pmatrix} 1 & 0 & 0 & 1 \end{pmatrix} & \begin{pmatrix} 0 & 1 & 0 & 1 \end{pmatrix} & \begin{pmatrix} 0 & 0 & 1 & 1 \end{pmatrix} \\
 \begin{pmatrix} 1 & 0 & 0 & -1 \end{pmatrix} & \begin{pmatrix} 0 & 1 & 0 & -1 \end{pmatrix} & \begin{pmatrix} 0 & 0 & 1 & -1 \end{pmatrix} \\
 \begin{pmatrix} -1 & 0 & 0 & 1 \end{pmatrix} & \begin{pmatrix} 0 & -1 & 0 & 1 \end{pmatrix} & \begin{pmatrix} 0 & 0 & -1 & 1 \end{pmatrix} \\
 \begin{pmatrix} -1 & 0 & 0 & -1 \end{pmatrix} & \begin{pmatrix} 0 & -1 & 0 & -1 \end{pmatrix} & \begin{pmatrix} 0 & 0 & -1 & -1 \end{pmatrix} \\
 \begin{pmatrix} 0 & 1 & 1 & 0 \end{pmatrix} & \begin{pmatrix} 1 & 0 & 1 & 0 \end{pmatrix} & \begin{pmatrix} 1 & 1 & 0 & 0 \end{pmatrix} \\
 \begin{pmatrix} 0 & 1 & -1 & 0 \end{pmatrix} & \begin{pmatrix} -1 & 0 & 1 & 0 \end{pmatrix} & \begin{pmatrix} 1 & -1 & 0 & 0 \end{pmatrix} \\
 \begin{pmatrix} 0 & -1 & 1 & 0 \end{pmatrix} & \begin{pmatrix} 1 & 0 & -1 & 0 \end{pmatrix} & \begin{pmatrix} -1 & 1 & 0 & 0 \end{pmatrix} \\
 \begin{pmatrix} 0 & -1 & -1 & 0 \end{pmatrix} & \begin{pmatrix} -1 & 0 & -1 & 0 \end{pmatrix} & \begin{pmatrix} -1 & -1 & 0 & 0 \end{pmatrix}
 \end{array} \quad (1)$$

This grouping of the lattice vectors into three subgroups of eight will be discussed further below. For now we note that, if $\theta(n_A, m_B)$ is the angle between the n th vector of group A and the m th vector of group B , then $\theta(n_A, m_B) = \theta(n_B, m_C) = \theta(n_C, m_A)$ and $\theta(n_A, m_A) = \theta(n_C, m_B) = \theta(n_C, m_C)$, and each group contains four oppositely oriented pairs of vectors. In other words, the ordering of the velocity vectors is such that group B is related to group A in exactly the same way as group C is related to B and A is related to C .

It is possible to visualize the FCHC lattice by the geometrical construction shown in Fig. 2. Consider four unit circles packed into a square of side 4 in two dimensions. It is straightforward to see that the inscribed circle tangent to each of these four unit circles has radius $\sqrt{2} - 1$. In three dimensions, when eight unit spheres are packed into a cube of side 4, the

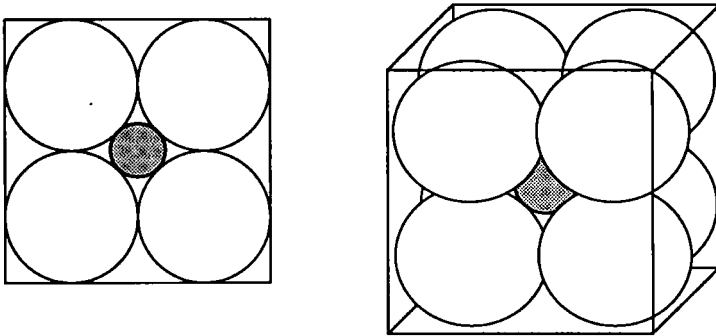


Fig. 2. Geometric method of visualization of the FCHC lattice. The $(2^2, 2^3)$ unshaded unit (circles, spheres) are packed into a (square, cube) of side 4. The shaded (circle, sphere) that is tangent to them has radius equal to one less than the square root of the number of dimensions.

inscribed sphere has radius $\sqrt{3} - 1$. Likewise, in D dimensions, when 2^D unit hyperspheres are packed into a hypercube of side 4, the inscribed hypersphere has radius $\sqrt{D} - 1$. In particular, in four dimensions ($D = 4$), the inscribed hypersphere is also a unit hypersphere. This nontrivial packing of unit hyperspheres provides an alternative description, within a factor of $\sqrt{2}$, of the FCHC lattice: the centers of the hyperspheres are the lattice vertices, and tangent hyperspheres correspond to linked vertices.

This geometrical description makes it clear that 16 of a given lattice site's neighbors lie on the corners of a perfect four-dimensional hypercube, while the other 8 neighbors correspond to the 8 faces of that hypercube.⁷ Presumably, this is how the face-centered hypercubic lattice derives its name. Note also that there are three distinct ways in which this partition of the lattice vectors into a group of 16 and a group of 8 may be carried out. These three ways correspond to letting each of the three subgroups in the list (1) be the group of eight.

To see this explicitly, note that the proper orthogonal matrix

$$A = \frac{1}{\sqrt{2}} \begin{pmatrix} +1 & +1 & 0 & 0 \\ +1 & -1 & 0 & 0 \\ 0 & 0 & +1 & +1 \\ 0 & 0 & +1 & -1 \end{pmatrix} \quad (2)$$

⁷ Recall that a D -dimensional hypercube has $2D$ faces.

when applied to each of the 24 lattice vectors in Eq. (1) yields⁸

$$\begin{array}{ccc}
 A & B & C \\
 (+1 \ +1 \ +1 \ -1) & (+1 \ -1 \ +1 \ -1) & (\ 0 \ 0 \ +2 \ 0) \\
 (+1 \ +1 \ -1 \ +1) & (+1 \ -1 \ -0 \ +1) & (\ 0 \ 0 \ 0 \ +2) \\
 (-1 \ -1 \ +1 \ -1) & (-1 \ +1 \ +1 \ -1) & (\ 0 \ 0 \ 0 \ -2) \\
 (-1 \ -1 \ -1 \ +1) & (-0 \ +1 \ -1 \ +1) & (\ 0 \ 0 \ -2 \ 0) \\
 (+1 \ -1 \ +1 \ +1) & (+1 \ +1 \ +1 \ +1) & (+2 \ 0 \ 0 \ 0) \\
 (+1 \ -1 \ -1 \ -1) & (-1 \ -1 \ +1 \ +1) & (\ 0 \ +2 \ 0 \ 0) \\
 (-1 \ +1 \ +1 \ +1) & (+1 \ +1 \ -1 \ -1) & (\ 0 \ -2 \ 0 \ 0) \\
 (-1 \ +1 \ -1 \ -1) & (-1 \ -1 \ -1 \ -1) & (-2 \ 0 \ 0 \ 0)
 \end{array} \quad (3)$$

In this representation, it is manifest that the lattice vectors of subgroups A and B lie at the corners of a perfect four-dimensional hypercube, and that those of subgroup C lie on its faces. In what follows, we therefore refer to this representation as the *explicit hypercubic frame*. This frame will be useful below for describing the isometries of the FCHC lattice.

Finally, we note that isotropic three-dimensional hydrodynamics can be obtained from three-dimensional projections of this four-dimensional lattice. Due to the staggered nature of the FCHC lattice, this requires only two lattice spacings in the fourth dimension. Alternatively (and equivalently), we can simply project out the fourth coordinate of the lattice vectors in Eq. (1). The resulting set of three-vectors are the lattice vectors of an irregular lattice in three dimensions. The neighbors of a point $(0, 0, 0)$ on this lattice can be described in Cartesian coordinates as the 6 on-axis neighbors at distance one $[(\pm 1, 0, 0), (0, \pm 1, 0), \text{ and } (0, 0, \pm 1)]$, each counted with multiplicity two (double bonds), and the 12 neighbors at distance $\sqrt{2}$ $[(\pm 1, \pm 1, 0) \text{ and permutations}]$. The four-tensor constructed by these lattice vectors is perfectly isotropic.

3.2. Microdynamics

The two basic steps of the LGA are (1) propagation of the particles and (2) collisions. The particles reside on the lattice sites only, and there can be at most one particle per direction at any given site and time. The hydrodynamic behavior of the model depends on the fact that the collision step conserves mass and momentum (conservation of these quantities holds trivially in the propagation step).

In order to introduce flow with solid walls present one must introduce new collisions which prevent particles from moving across the boundaries.

⁸ For brevity, we have omitted the normalization factor $1/\sqrt{2}$ in front of each of these vectors.

These might be either of the bounce-back type, which send particles back into the direction from which they came, or of the mirror-reflection type, where only one component of the particle's momentum is changed. When particle velocities are averaged the effect of the bounce-back collision is a hydrodynamic no-slip boundary condition.^(23, 24) We shall use the bounce-back condition in the following, and we shall refer to the sites where this condition is implemented as *solid sites*.

In order to introduce a body force like gravity, an additional collision step is needed that puts momentum into the system. This can be done in several ways, one of which is to flip particle velocities at a few randomly chosen sites into the direction of the forcing.

The state at a single site (at position \mathbf{x} at time t) is given by the 24 occupation numbers $n_i(\mathbf{x}, t) \in \{0, 1\}$, which are simply the particle numbers in direction i . The time development of the n_i is given by the microdynamical equation

$$n_i(\mathbf{x} + \mathbf{c}_i, t + 1) = n_i(\mathbf{x}, t) + \Omega_i(\{\mathbf{n}(\mathbf{x}, t)\}) \quad (4)$$

The term $\Omega_i(\{\mathbf{n}(\mathbf{x}, t)\})$, where $\mathbf{n} = (n_1, n_2, \dots, n_{24})$, is the change in n_i due to collisions, \mathbf{c}_i are the velocity vectors connecting neighboring lattice sites, t is the time, and the time increment corresponding to a combined propagation and collision step is unity.

The full detailed state of the lattice gas is given by the set of all n_i on all sites. In simulations on a computer, all this information is packed into 24 bits of information at each site, and is stored and updated. However, the quantities of physical interest are the (space and/or time and/or ensemble) averaged mass and momentum densities. On the CAM-8 this averaging can be performed by the application of lookup tables and read to the front end without loss of speed.

3.3. The 16-Bit Collision Operator and Random Isometries

In a three-dimensional lattice gas the number of possible collision rules, represented by the collision operator Ω , is very large. If one 24-bit output configuration for each of the $2^{24} = 16\text{M}$ input configurations were stored in a table, the table would have a size of at least 48 Mbytes. This is bigger than what the local SRAM memory in each node of the CAM-8 permits, and it is also bigger than the local memory of some massively parallel machines, like the Connection Machine CM2. The restriction for the CAM-8 is the 16-bit limit of the lookup tables. In order to adapt to this restriction each 24-bit collision is split into two 16-bit collisions. The structure of this factorization is shown in Fig. 3. The particle velocities are split

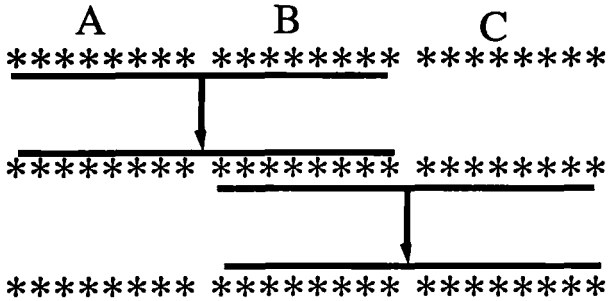


Fig. 3. The structure of the two-step collisions. Each asterisk represents a particle occupation number (a bit). The arrows show which bits are influenced by each collision step.

into the three groups of eight introduced in Eq. (1). The collisions, which are given by a single table, involve 16 particles at a time and act first on the first 16 particles (subgroups *A* and *B*) and then on the last 16 (subgroups *B* and *C*). The overall mass and momentum of the 16 particles are conserved at each step. The 16-bit table is constructed so that each output state corresponds to only one input state. In other words, the table can be considered as a one-to-one map between the sets of output and input states. Consequently, the 24-bit collision table that results from combining two copies of the 16-bit table will also be a one-to-one map. For this reason the collisions satisfy semi-detailed balanced.⁽⁵⁾

Such a division of the collision rule into three fixed sets of spatial directions can introduce anisotropies. Indeed, these collision rules give rise to a viscosity which varies by more than 20% with the direction of the velocity gradients. In order to prevent this effect, the particles are first subjected to a random precursor transformation—an isometry p —before the collision *C*; after the collision they are then subjected to the inverse isometry p^{-1} . The isometries p form a group G defined as the set of transformations that map the set of lattice vectors $\{\mathbf{c}_i\}$ to itself, preserving the vectors' lengths and the angles between them. The total collision step can thus be represented by the operator $p^{-1}Cp$, where C is deterministic and is given by the 16-bit table, and p is randomly chosen from the isometry group G at every timestep. Since the group of p 's include all possible spatial rotations, and since they are chosen randomly at each timestep, it is clear that their effect will be to average out all anisotropies in the collision table. Note that p can be the same for all sites on the lattice.

It can be shown that there are altogether 1152 elements in G ,⁽¹⁸⁾ and each element is a map acting on all the 24 bits. It is therefore crucial that the isometries can be factorized into factors that, like C , decompose into operations on subsets of the 24 bits.

This factorization takes a convenient form when specified by the action of the isometries on the coordinates of the velocity vectors in the explicit hypercubic frame defined by Eq. (1). In this frame the isometries take the form of a product of simple coordinate inversions and permutations, known as R and P isometries, respectively, combined with the forward or reverse cyclic interchange of the subgroups A , B , and C .⁽¹⁷⁾ Specifically, the isometries corresponding to the forward $[(A, B, C) \rightarrow (C, A, B)]$ and reverse $[(A, B, C) \rightarrow (B, C, A)]$ cyclic interchange of the three subgroups are denoted by S_1 and S_2 , respectively. The R and P isometries are particularly simple because they do not map vectors between $A+B$ and C . Thus they can be encoded as 16-bit and 8 bit tables acting on $A+B$ and C , respectively.

As a concrete example, consider the axis-inversion isometry R_4 , implemented by negating the fourth coordinate in the explicit hypercubic frame. As before, we enumerate the lattice vectors in this frame by $1_A, \dots, 8_A, 1_B, \dots, 8_B, 1_C, \dots, 8_C$, where, for example, n_A denotes the n th entry of column A in Eq. (3). It is evident that the application of R_4 amounts to swapping the lattice vectors 1_A and $5_B, 2_A$ and $7_B, 3_A$ and $6_B, 4_A$ and $8_B, 5_A$ and $1_B, 6_A$ and $2_B, 7_A$ and $3_B, 8_A$ and 4_B , and 2_C and 3_C . The orthogonal matrix, Eq. (2), then maps these swaps back to the corresponding swaps in the original frame, Eq. (1), even though it is evident that R_4 is no longer a simple axis inversion in that frame. So, for example, ordering the lattice vectors and their corresponding bits according to Eq. (1), we see that the state

$$1010101010101010101010 \tag{5}$$

maps to the state

$$110010101010110011001010 \tag{6}$$

under the isometry R_4 .

To apply a general isometry p to the lattice, we exploit the fact that p can be written in the product form

$$\begin{pmatrix} I \\ S_1 \\ S_2 \end{pmatrix} \begin{pmatrix} I \\ R_1 \end{pmatrix} \begin{pmatrix} I \\ R_2 \end{pmatrix} \begin{pmatrix} I \\ R_3 \end{pmatrix} \begin{pmatrix} I \\ R_4 \end{pmatrix} \begin{pmatrix} I \\ P_{12} \end{pmatrix} \begin{pmatrix} I \\ P_{13} \\ P_{23} \end{pmatrix} \begin{pmatrix} I \\ P_{14} \\ P_{24} \\ P_{34} \end{pmatrix} \tag{7}$$

where the indices of the R and P isometries refer to the axis to be inverted or the axes to be permuted, respectively. The elementary R and P isometries are their own inverses, whereas S_1 is the inverse of S_2 . To choose a random

isometry at each time step, eight random numbers are computed and used to choose one isometry from each column above. The resulting combined isometry is then performed by the successive application of tables corresponding to each of the elementary isometries. The inverse isometry is obtained by the application of the tables in the reverse order.

3.4. Memory Usage and Implementation of the Algorithm

The memory in the CAM-8 is arranged so that there are four 16-bit subcells at each lattice site. The initial organization of the memory is to occupy the first eight bits of the first three subcells with the three groups A , B , and C of lattice vectors, respectively. The subcells are given the same labels, A , B , and C , as the velocity groups they contain. The extra bits are used as logical flags and swap space which can minimize the number of steps required to implement the collision algorithm, trading abundant memory for computational speed. In addition, there is a subcell D which contains flags that indicate whether or not a lattice site is solid, and whether or not forcing is to be performed (if possible) at that site. Thus bits 0–7 of the subcell A indicate the presence or absence of particles moving in lattice directions A , while bits 0–7 of subcell B indicate similarly for lattice directions B , and bits 0–7 of subcell C indicate similarly for lattice directions C .

The collision algorithm proceeds in five steps:

1. Apply forcing and reorganize the memory to prepare subsequent steps.
2. Apply randomly chosen R , P , and S isometries.
3. Apply collision table.
4. Apply inverses of isometries applied in step 2 in reverse order.
5. Reflect lattice vectors at solid sites and restore initial organization of memory.

Forcing is applied by adding momentum to a particle if possible and if the flag at the site permits. The bit-field of flags (or bit-fields, if forcing in more than one direction is done simultaneously) is randomly shifted at each time step so that forcing is on average uniform over the space. Because the same lookup tables are necessarily applied at every site, the amount of forcing is set in the initial conditions by setting the number of positively set flags. The amount of forcing applied cannot be precisely tuned, since not all particle configurations can be changed to increase the momentum in a given direction. For this reason the applied force must be measured along with the other observables.

At the solid sites all momenta are reversed. This is an operation that can be performed on each of the three groups of bits separately, since each group contains four pairs of oppositely oriented momenta. The momentum reversals are handled in the following manner. The flag that indicates whether or not a site is solid is copied into each of the first three subcells. If the site is solid, the momentum information in each subcell (in bits 0–7) is moved to the higher eight bits (8–15) and the lower bits are set to zero. The subsequent steps in the collision algorithm are thus applied to the eight bits of zero instead of the momentum information, and the net result is no change. At the end of the collision step, the presence of zeros in the first eight bits of each subcell indicates that the site is solid, and that the momentum information in the high eight bits should be reflected through the origin and repositioned in the lower eight bits of each subcell. This algorithm is robust in the case where the site is not solid but no particles are present, since, in this case, the reflection of the bits will cause no change.

When forcing is being applied in only a single direction, the collision algorithm requires 26 applications of lookup tables when an S isometry is applied, and 14 applications when the S isometry chosen is the identity, which happens 33% of the time. Thus the average number of lookup table applications required per time step is 22. The performance of the present algorithm on the eight-node machine (one node handles 4M 16-bit sites) is 7M site updates per second. It benefits greatly from the fact that the CAM-8 can download one table while being busy using another, without loss of speed.

4. OPTIMIZATION OF THE VISCOSITY

Typically, lattice-gas collision rules are chosen to maximize a “Reynolds coefficient” and thus the Reynolds number of a simulation. For the application we envision—namely, slow flow through disordered porous media—accuracy and efficiency of the simulation improve as the kinematic viscosity is reduced.⁽²⁵⁾ In this section we show how we choose our 16-bit collision tables to obtain a low viscosity.

By employing the Boltzmann approximation, which assumes that the particles entering a collision are uncorrelated, it is possible to derive a closed expression for the kinematic viscosity ν in terms of the collision rules and the average density $d \leq 1$ per direction i . The formula, due to Hénou,⁽¹⁸⁾ has the form

$$\nu = \frac{1 + Q}{6(1 - Q)} \quad (8)$$

where

$$Q = \frac{1}{18} \sum_{ss'} A(s \rightarrow s') d^{m-1} (1-d)^{23-m} Y_{\alpha\beta}(s) Y_{\alpha\beta}(s') \quad (9)$$

and $A(s \rightarrow s')$ is the probability that the state s goes into s' . The sum runs over all possible input and output states s and s' , where $s = \{s_i\}$, $m = \sum_i s_i$ is the mass at a site, α and β are Cartesian indices with summation over repeated indices implied, and

$$Y_{\alpha\beta} = \sum_{i=1}^{24} s_i (c_{i\alpha} c_{i\beta} - \frac{1}{2} \delta_{\alpha\beta}) \quad (10)$$

where $\delta_{\alpha\beta}$ is the Kronecker delta. The sum (9) is not as hard to compute as it may appear. First, note that the term $Y_{\alpha\beta}(s) Y_{\alpha\beta}(s')$ is easily evaluated as

$$\begin{aligned} Y_{\alpha\beta}(s) Y_{\alpha\beta}(s') &= \sum_{ij} s_i s'_j (c_{i\alpha} c_{i\beta} - \frac{1}{2} \delta_{\alpha\beta}) (c_{j\alpha} c_{j\beta} - \frac{1}{2} \delta_{\alpha\beta}) \\ &= \sum_{ij} s_i s'_j [(\mathbf{c}_i \cdot \mathbf{c}_j)^2 - 1] \\ &= \sum_{ij} s_i s'_j \mathcal{A}_{ij} \end{aligned} \quad (11)$$

where

$$\mathcal{A}_{ij} = (\mathbf{c}_i \cdot \mathbf{c}_j)^2 - 1 \quad (12)$$

Furthermore, the random isometries cancel themselves out. To see this, note that the probability $A(s, s')$ can be written

$$A(s, s') = \frac{1}{1152} \sum_p A_0(ps, ps') \quad (13)$$

where p is an isometry and

$$A_0(s, s') = \begin{cases} 1 & \text{if } s' = Cs \\ 0 & \text{otherwise} \end{cases} \quad (14)$$

where Cs is the output of the deterministic 24-bit collision table. From Eq. (9) it then follows that

$$Q = \sum_{s, s'} f_d A(s, s') Y_{\alpha\beta}(s) Y_{\alpha\beta}(s') \quad (15)$$

$$= \frac{1}{1152} \sum_{p, s, s'} f_d A_0(p s, p s') Y_{\alpha\beta}(s) Y_{\alpha\beta}(s') \quad (16)$$

$$= \frac{1}{1152} \sum_{p, s} f_d Y_{\alpha\beta}(s) Y_{\alpha\beta}(p^{-1} C p s) \quad (17)$$

$$= \frac{1}{1152} \sum_{p, s} f_d Y_{\alpha\beta}(p^{-1}) Y_{\alpha\beta}(p^{-1} C s) \quad (18)$$

$$= \frac{1}{1152} \sum_{p, s} f_d Y_{\alpha\beta}(s) Y_{\alpha\beta}(C s) \quad (19)$$

$$= \sum_s f_d Y_{\alpha\beta}(s) Y_{\alpha\beta}(C s) \quad (20)$$

where $f_d = d^{m-1}(1-d)^{23-m}$, and in passing from Eq. (18) to (19), we have used the fact that isometries preserve inner products and that the product $Y_{\alpha\beta}(s) Y_{\alpha\beta}(s')$ depends only on inner products of vectors. The latter property may be deduced from Eq. (12) by noting that $Y_{\alpha\beta}(s) Y_{\alpha\beta}(s') = m^2[(\mathbf{u} \cdot \mathbf{u}')^2 - 1]$, where the velocities \mathbf{u} and \mathbf{u}' correspond to states s and s' , respectively.

The minimization of Eq. (9) may be made clearer by noting that the angle between lattice vectors i and j in different subgroups of \mathcal{A}_{ij} is either $\pi/3$ or $2\pi/3$, and $|\mathbf{c}_i| = \sqrt{2}$. It follows that $\mathbf{c}_i \cdot \mathbf{c}_j = \pm 1$ and that $\mathcal{A}_{ij} = 0$ for i and j in different subgroups. It follows that the 24×24 matrix \mathcal{A} is block diagonal,

$$\mathcal{A} = \begin{pmatrix} A & 0 & 0 \\ 0 & A & 0 \\ 0 & 0 & A \end{pmatrix} \quad (21)$$

where the 0's denote 8×8 null matrices, and the 8×8 matrix of components A for lattice vectors in the same subgroup is given by

$$A = \begin{pmatrix} +3 & -1 & -1 & +3 & -1 & -1 & -1 & -1 \\ -1 & +3 & +3 & -1 & -1 & -1 & -1 & -1 \\ -1 & +3 & +3 & -1 & -1 & -1 & -1 & -1 \\ +3 & -1 & -1 & +3 & -1 & -1 & -1 & -1 \\ -1 & -1 & -1 & -1 & +3 & -1 & -1 & +3 \\ -1 & -1 & -1 & -1 & -1 & +3 & +3 & -1 \\ -1 & -1 & -1 & -1 & -1 & +3 & +3 & -1 \\ -1 & -1 & -1 & -1 & +3 & -1 & -1 & +3 \end{pmatrix} \quad (22)$$

Thus, heuristically speaking, collision events that take a particle from one lattice vector to another—neither the original one nor its negation—in the same subgroup of eight are the most preferred in terms of minimizing Q , since in these cases the score, computed from Eq. (12), is -1 . Collisions that take a particle to a different subgroup are next (score = 0). Finally, collisions that take particles to themselves or their negation are least preferred (score = +3). The collision set that minimizes this scoring is optimal.

Due to the symmetric ordering of the velocity vectors, Q splits into a sum of three terms

$$Q = Q_A + Q_B + Q_C \quad (23)$$

corresponding to the group, A , B , and C respectively. We consider only the first two terms, which corresponds to a 16-bit table, and choose the collisions that minimize $(Q_A + Q_B)$. Note that $v = v(Q)$ is an increasing function of Q , so that minimizing Q is equivalent to minimizing μ . Minimizing $(Q_A + Q_B)$, however, is not equivalent to minimizing $Q_A + Q_B + Q_C$. The former quantity results from a single application of the 16-bit table, whereas the latter quantity results from applying the 16-bit table twice. Only Q_A remains the same after the second application.

The reason for doing only the restricted optimization is twofold. First, by restricting the optimization to the 16-bit space with 2^{16} velocities, an exhaustive search through all possible output states corresponding to every input state is feasible and requires only about 1 h of computation time on a Sun Sparcstation 2. By comparison, an exhaustive search through all output states corresponding to the 2^{24} possible input states of the complete collision table would require increasing computation time by a factor of $(2^8)^2 \approx 65,000$.

Second, we argue that the process of minimizing $Q_A + Q_B$ approximates the process of minimizing Q . From the above equations it is seen that minimizing Q means finding output states that select the matrix elements -1 in A . This corresponds to maximizing the number of perpendicular directions between the velocities of the input and output states within each subgroup of eight. Physically it corresponds to minimizing the momentum flux and thereby the viscosity. For this purpose it is advantageous to let a particle scatter into one of the directions of its own subgroup which give a contribution -1 to the matrix product, rather than into another subgroup, which would give no contribution to the matrix product. The 16-bit collisions certainly allow for the particles to go into their own subgroups.

However, the selection of output states is restricted, not only by mass and momentum conservation, but by the limited number of velocities in the

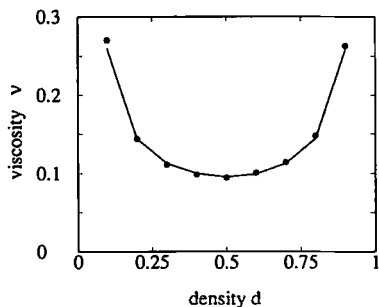


Fig. 4. Viscosity ν as a function of the reduced density d . The line shows the Boltzmann values and the dots show the values obtained from simulations.

16-bit states as well. Also, since the 16-bit table is applied twice to give the full collision, the eight particles that are involved in both collisions may scatter back into a disadvantageous direction. The probability that such backscattering occurs, however, appears to be small enough to give a relatively low viscosity. A refined scheme that takes into account that the 16-bit collisions are indeed applied twice would be expected to decrease the viscosity further. However, it would not circumvent the severe restrictions intrinsic to a 16-bit table. In optimization schemes^(19, 20) that employ the freedom to pick output states in the full space of 24-bit states, the viscosity is reduced to values which are almost an order of magnitude smaller than those we report here.

Our optimized viscosity, determined from the Boltzmann approximation of Eqs. (8)–(10), is given as a function of the reduced density d in Fig. 4. Here it is also compared to measurements of the viscosity by simulation of a relaxing shear wave on the CAM-8. Specifically, simulations were initialized with the velocity profile

$$u_z(x, t = 0) = U \sin(kx) \tag{24}$$

where u_z is the z component of the velocity, $k = 2\pi/L$, $L = 64$ is the linear size of the system, $U = 0.07$ is the maximum flow velocity, x is a Cartesian coordinate, and t is the time. According to the Stokes equation, the velocity should evolve as

$$u_z(x, t) = U \sin(kx) \exp(-k^2 \nu t) \tag{25}$$

The viscosity can thus be deduced from the integral $\int_0^L dx |u_z|$, which decays exponentially with time. In Fig. 4, error bars are approximately the size of the symbols. The measured values are expected to be somewhat greater than the Boltzmann prediction^(26, 20, 27) and indeed most of our measurements

are. The fact that some are not is indicative of the magnitude of the experimental error.

The minimum viscosity is obtained at a density $d=0.5$ and has the value $\nu=0.095$. For comparison, the value obtained from a purely random table is $\nu=0.1667$. When Q is minimized by choosing the collisions by an exhaustive search in the (severely) restricted space of 24-bit *isometries*,⁽¹⁸⁾ the resulting viscosity is within 20% of the value resulting from the random table.⁹

5. TEST SIMULATIONS

To check the behavior of the model when the fluid is forced in the presence of solid walls we performed simulations of flow through a pipe and channel as well as flow through a simple cubic array of solid spheres. The latter geometry creates the only truly three-dimensional flow because the flow passes through constrictions. The simulations of pipe flow were carried out to obtain an estimate of the lower limit for the spatial size of obstructions and constrictions.

Table I summarizes the results of the simulations of flow through channels of half-width R , pipes with radius R , and periodic cubic arrays of spheres with radius R . The pipes were constructed with periodic boundary conditions in the flow direction, whereas the channels had periodic boundaries in two directions and a flat-wall boundary perpendicular to the third direction. In the table, the permeability κ of each particular geometry is compared to the theoretical prediction of the permeability κ_{theory} . The permeability is defined as

$$\kappa = \frac{J\nu\phi}{F} \quad (26)$$

where J is the total mass flux, F is the total force applied to the fluid, and ϕ is the fraction of void space, i.e., the porosity. Note that $\phi=1$ for the pipe and the channel. In the simulations the permeabilities were deduced from the measurement of the average flow rate and the average forcing of the fluid, and the uncertainties are estimated from the noise in these data.

The theoretical expression for the permeability of the pipe,

$$\kappa_{\text{theory}} = \frac{R^2}{8} \quad (27)$$

⁹ In this case the problem is slightly different because the minimization is of a Reynolds coefficient rather than of the viscosity.

Table I. Comparison of Calculations of the Permeability κ to Theoretical Predictions κ_{theory} for Channels, Pipes, and a Periodic Cubic Array of Spheres^a

Geometry	ϕ	R	$(\kappa - \kappa_{\text{theory}})/\kappa_{\text{theory}}$	R_{eff}
Channel	1.0	1.5	$+0.04 \pm 0.03$	1.6
	1.0	2.5	-0.04 ± 0.02	2.4
	1.0	3.5	-0.03 ± 0.05	3.4
	1.00	7.5	$+0.03 \pm 0.05$	7.7
	1.00	15.5	$+0.04 \pm 0.05^*$	16.1
Pipe	1.0	1.5	$+0.09 \pm 0.07$	1.6
	1.0	2.5	$+0.01 \pm 0.04$	2.5
	1.0	8.5	-0.03 ± 0.02	8.4
	1.0	15.5	$-0.07 \pm 0.05^*$	14.9
Array of spheres	0.713	4.5	-0.07 ± 0.08	4.6
	0.907	4.5	-0.11 ± 0.02	4.7
	0.719	6.5	$+0.05 \pm 0.06$	6.4
	0.882	19.5	$-0.12 \pm 0.04^*$	20.4
	0.882	19.5	-0.04 ± 0.02	19.8
	0.735	25.5	$-0.04 \pm 0.07^*$	25.8

^a R denotes the radius of the pipes and spheres and the half-width of the channels, R_{eff} denotes the effective radius (half-width) corresponding to the theoretical expressions for κ_{theory} ; ϕ is the void fraction. The asterisk shows the simulations that were performed on CAM-8. The remaining small-scale simulations were carried out on a workstation.

is easily obtained from the Stokes equation, as is the permeability of a channel

$$\kappa_{\text{theory}} = \frac{R^2}{3} \tag{28}$$

The theoretical expression for the permeability of the simple cubic array of spheres is obtained (in a slightly different form) by Hasimoto⁽²⁸⁾ and Sangani and Acrivos⁽²⁹⁾ and has the form

$$\kappa_{\text{theory}} = \frac{2}{9K(\phi)} \left(\frac{\phi}{1-\phi} \right) R^2 \tag{29}$$

where $K(\phi)$ is given in ref. 29. In this case the radii $R=19.5$ and 26.5 correspond to the porosities $\phi=0.882$ and $\phi=0.735$, respectively. The drag F on a single sphere in the array is

$$F = K(\phi) 6\pi\rho\nu R \tag{30}$$

where ρ is the mass density and ν is the viscosity of the fluid. It is seen that $K(\phi) \geq 1$ is the correction factor to the Stokes law. When the spheres are infinitely far apart $\phi = 1$ and $K = 1$.

The noninteger values of R are discussed below. They are related to the definitions of the (discretized) geometries in the following way: For the pipe a site will be a void site if its distance r from the symmetry axis satisfies the inequality

$$r < R + 0.5 \quad (31)$$

The remaining sites on the lattice will be solid sites. The solid sites of the sphere are given by the same inequality if r is taken to be the distance from the center of the sphere.

The effective radius R_{eff} given in Table I is the radius (half-width) that gives the observed permeability when inserted in the theoretical expressions for κ_{theory} . Especially in the case of the spheres the permeability varies strongly with R , and the difference between R and R_{eff} corresponding to the discrepancies between κ and κ_{theory} is small.

The discrepancies between the theoretical and simulated results have three principal causes:

- Uncertainty in the effective position of the wall
- Discretization errors
- Effects of compressibility

In the case of the channel and pipe simulations, only the first and second problems come into play, whereas all three cause errors in the three-dimensional case of the spheres. The discretization errors are due both to the approximations made when smoothly curved surfaces are represented on a lattice and to nonhydrodynamic effects at sufficiently small scales.

For the hydrodynamic behavior of the lattice gas to be described by the equations of incompressible hydrodynamics, several requirements must be fulfilled. First, the geometry must be such that there is a scale separation between the lattice constant and the scale over which the flow varies. The ratio between these scales is denoted by the small number ε . Second, the flow must be forced sufficiently weakly so that the flow velocity u does not exceed ε . Finally, density variations must remain small. More precisely, the variations in ρ must be of order ε^2 or smaller. In geometries where the overall permeability is small, a relatively large force will be necessary to drive the flow and spatial variations in the permeability (caused, for instance, by constrictions) may result in large density variations, even when u is small.

This is the case in particular for the CAM-8 simulation with the $R = 19.5$ sphere where the forcing applied produced a maximum flow velocity $u = 0.10$.

This simulation was repeated on a workstation with approximately half the forcing, and the resulting discrepancy between theory and simulations was correspondingly decreased.

When the requirements on the scale separation are obeyed and there is no forcing, the lattice gas is described by ⁽²²⁾

$$\frac{\partial \mathbf{u}}{\partial t} + g(\rho) \mathbf{u} \cdot \nabla \mathbf{u} = -\frac{\nabla P}{\rho} + \nu \nabla^2 \mathbf{u} \tag{32}$$

where \mathbf{u} and ρ are the average flow velocity and the density, respectively,

$$P = (1/2) \rho [1 - g(\rho) u^2] \tag{33}$$

is the pressure, ⁽²²⁾ and ν is the kinematic viscosity. The g -factor is given as

$$g(\rho) = \frac{4}{3} \left(\frac{12 - \rho}{24 - \rho} \right) \tag{34}$$

The velocity dependence in the pressure results from the discreteness of the velocities and the exclusion principle. For the purpose of finite-Reynolds-number simulations, the g -factor may be removed by rescaling the velocity as $u' = g(\rho)u$.⁽²²⁾ In the simulations the average density $\bar{\rho} = 12$ was chosen so that $g = 0$ and the flow is described by the Stokes equation in the limit where there are no density variations.

As an example of how to quantify the density variations in steady-state flow, we give an estimate of the density variations that will result in the case of the array of spheres. By the above equation of state (33) we have that the density difference across the sphere is given as

$$\Delta \rho \approx 2 \Delta P \tag{35}$$

But this pressure difference can be estimated as the drag divided by some area which is characteristic for the sphere, say πR^2 . Hence, by Eq. (30)

$$\Delta \rho \approx K(\phi) \cdot 12 \nu U / R \tag{36}$$

Since the drag coefficient $K(\phi)$ increases sharply with decreasing porosity ϕ , $\Delta \rho$ may become significant even when $U/R \sim \varepsilon^2$ is small. Care must be taken in order for this effect of compressibility in the lattice gas to be negligible. In the present case when ρ is chosen so that $g(\rho) = 0$ and the Stokes equations are simulated, deviations in ρ from its average value will cause a finite value of $g(\rho)$. This means that the g -dependent term of Eq. (32) must be taken into account and we are no longer in the regime of linear hydrodynamics.

The effective wall positions have been studied theoretically by several authors.^(23, 24) It can be shown (theoretically) that in the case of Couette flow along a flat wall oriented in a direction parallel to the lattice directions, the position of vanishing velocity is not on the wall sites, but rather half a lattice unit measured from the wall sites into the fluid region. In the case when the velocity field has a nonvanishing second derivative, there is a correction to the effective wall position of relative order ε . This correction is significant only when the constrictions in the flow are very small, and it depends on the viscosity.

In the channel flow simulations referred above, we fitted the velocity profiles with a parabola, as predicted by the Stokes equation. Within the noise of the measurements we found agreement between simulations and a parabolic profile going through the position halfway between the first wall site and the first fluid site. We also found good agreement when the wall normal was in an angle of $\pi/4$ to the closest lattice directions. This result slightly generalizes the predicted result for the wall positions⁽²⁴⁾. In Table I the values of R are obtained by assuming that the effective wall position is always halfway between the first wall site and the first fluid site. In the case of curved geometries this approximation creates discrepancies in addition to the discretization approximation.

The relatively good agreement between theory and simulations in the case of the two smallest pipes is coincidental, since the cross sections of these pipes are squares rather than circles. In simulations of the flow around the periodic array of spheres (in the simulations, a single sphere and periodic boundary conditions were used) the result is highly sensitive to the exact position of the boundary, as can be seen from the values of R_{eff} given in Table I, and the small discrepancy between simulation and theory can be accounted for by a correspondingly small shift of the effective boundary.

In general, the lower limit on the size of obstructions and constrictions depends on the particular application as well as the required precision. In the case of flow in porous media, the coarse-grained characteristics depend mainly on the flow in the widest channels, and the averaged behavior depends only weakly on the flow in the narrower passages through the medium. In this case the small-scale hydrodynamics may not matter much. But the permeability typically depends strongly on the effective positions of the walls, and care must be taken to ensure that these are correctly represented or that the channels are sufficiently wide.

6. CONCLUSION

We have designed an algorithm for the implementation of a three-dimensional (FCHC) lattice gas model on the CAM-8. It has been shown

how a proper geometric grouping of the velocity vectors on the lattice makes it possible to decompose both the collisions and the random isometries acting on the full 24-bit states into operations involving only 16 or 8 bits at a time. The corresponding 16-bit collision table has been optimized to obtain a minimum viscosity, and tested against analytic results from the Boltzmann theory. The architecture of the CAM-8 has been described, and the performance of an eight-node machine has been shown to be comparable to that of existing supercomputers. Some practical limitations of the model have been established and discussed, and it has been shown that the model behaves according to the hydrodynamic predictions for various permeable media. We have thus demonstrated that this implementation of the FCHC lattice gas represents a working tool for large-scale simulation of flows in simple and complex geometries.

ACKNOWLEDGMENTS

We thank John Olson for helpful discussions. One of us (B.M.B.) would like to acknowledge helpful conversations with David Levermore and Washington Taylor. This work was supported in part by the sponsors of the MIT Porous Flow Project and NSF grant 9218819-EAR. E.G.F. acknowledges support by NFR, the Norwegian Research Council for Science and the Humanities. The CAM-8 project is supported by ARPA under grant N00014-94-1-0662.

REFERENCES

1. S. Wolfram, ed., *Theory and Applications of Cellular Automata* (World Scientific, Singapore, 1986).
2. T. Toffoli and N. Margolus, *Cellular Automata Machines* (MIT Press, Cambridge, Massachusetts 1987).
3. G. Weisbuch, *Complex Systems Dynamics* (Addison-Wesley Reading, Massachusetts, (1991).
4. U. Frisch, B. Hasslacher, and Y. Pomeau, *Phys. Rev. Lett.* **56**:1505-1508 (1986).
5. U. Frisch, D. d'Humières, B. Hasslacher, P. Lallemand, Y. Pomeau, and J.-P. Rivet, *Complex Systems* **1**:648 (1987).
6. D. H. Rothman, *Geophysics* **53**:509-518 (1988).
7. A. J. C. Ladd and M. E. Colvin, *Phys. Rev. Lett.* **60**:975-978 (1988).
8. M. Van der Hof and D. Frenkel, *Phys. Rev. A* **41**:4277 (1990).
9. D. H. Rothman and J. Keller, *J. Stat. Phys.* **52**:1119 (1988).
10. C. Appert and S. Zaleski, *Phys. Rev. Lett.* **64**:1 (1990).
11. D. H. Rothman and S. Zaleski, *Rev. of Mod. Phys.* **66**:1417-1479 (1994).
12. N. Margolus, T. Toffoli, and G. Vichniac, *Phys. Rev. Lett.* **56**:1694-1697 (1986).
13. A. Clouqueur and D. d'Humières, *Complex Systems* **1**:584-597 (1987).
14. D. d'Humières, P. Lallemand, and U. Frisch, *Europhys. Lett.* **2**:291 (1986).

15. N. Margolus and T. Toffoli, Cellular-automata machines, in *Lattice-Gas Methods for Partial Differential Equations*, in G. Doolen, ed. (Addison-Wesley, Reading, Massachusetts, 1990), pp. 219–249.
16. N. Margolus, Cam-8: A computer architecture based on cellular automata, in *Pattern Formation and Lattice-Gas Automata* A. Lawniczak and R. Kapral, eds. (American Mathematical Society, Providence, Rhode Island, 1995).
17. M. Hénon, *Complex Systems* 1:475–494 (1987).
18. M. Hénon, *Complex Systems* 1:763–789 (1987).
19. M. Hénon, Optimization of collision rules in the FCHC lattice gas, and addition of rest particles, in *Discrete Kinetic Theory, Lattice-Gas Dynamics, and Foundations of Hydrodynamics*, R. Monaco, ed. (World Scientific, Singapore, 1989), p. 146.
20. J. A. Somers and P. C. Rem, Obtaining numerical results from the 3D FCHC-lattice gas, in *Springer Proceedings on Physics, Workshop on Numerical Methods for the Simulation of Multi-Phase and Complex Flow* (Springer-Verlag, Berlin, 1992), pp. 59–78.
21. J. Hardy, O. de Pazzis, and Y. Pomeau, *Phys. Rev. A* 13:1949–1961 (1976).
22. G. D. Doolen, ed., *Lattice Gas Methods for Partial Differential Equations* (Addison-Wesley, Reading, Massachusetts, 1991).
23. R. Cornubert, D. d’Humières, and D. Levermore, *Physica D* 47:241 (1991).
24. I. Ginzbourg and P. M. Adler, *J. Phys. II France* 4:191–214 (1994).
25. B. Ferréol and D. H. Rothman, Lattice-Boltzmann simulations of flow through Fontainebleau sandstone, *Transport Porous Media*, in press (1995).
26. B. Dubrulle, U. Frisch, M. Hénon, and J.-P. Rivet, *J. Stat. Phys.* 59:1187–1226 (1990).
27. V. Coevorden, M. Ernst, and J. Somers, *J. Stat. Phys.* 74:1085 (1994).
28. H. Hasimoto, *J. Fluid Mech.* 5:317 (1959).
29. A. S. Sangani and A. Acrivos, *Int. J. Multiphase Flow* 8:343 (1982).